J. Fluid Mech. (2003), *vol.* 486, *pp.* 51–77. © 2003 Cambridge University Press
DOI: 10.1017/S0022112003004403 Printed in the United Kingdom

Planar velocity measurements in a weakly compressible mixing layer

By MICHAEL G. OLSEN† AND J. CRAIG DUTTON
Department of Mechanical and Industrial Engineering University of Illinois at Urbana-Champaign,
Urbana, IL 61801, USA

(Received 3 November 1999 and in revised form 7 January 2003)

High-vector-density planar velocity fields were obtained for a weakly compressible mixing layer using particle image velocimetry (PIV). The velocity ratio of the mixing layer was 0.53, the density ratio was 0.67, and the convective Mach number was 0.38. At the location where the PIV images were obtained, $Re_x = 3.7 \times 10^6$ and $Re_{\delta_\omega} = 1.8 \times 10^5$. The instantaneous planar velocity fields fall into three regimes characterized by the size and number of large-scale structures present. The large-scale rollers are either circular or elliptical, with the elliptical rollers having, in general, horizontal major axes. The transverse velocity fluctuations and Reynolds shear stress are suppressed for the weakly compressible mixing-layer as compared to the incompressible case. The spatial correlations of velocity fluctuations also occupy a smaller fraction of the mixing-layer thickness than for an incompressible mixing layer. The linear stochastic estimate of a roller structure is elliptical with the major axis oriented in the streamwise direction and with an eccentricity greater than for the incompressible case. The linear stochastic estimate of a braid suggests that the braids are vertically oriented, as opposed to the oblique orientation seen in incompressible mixing layers. In addition, the braids in the weakly compressible case have a vertically oriented stagnation line, as opposed to the braids in the incompressible mixing layer where stagnation occurs at a point.

1. Introduction

Although it is a geometrically simple flow field, the mixing layer (or shear layer) is of great practical importance since it appears often in engineering practice. The boundary region of a jet, the slip-stream behind a wing, and the interface between a recirculation region and a free stream are just a few examples of flow fields containing mixing layers. A typical geometry for a mixing-layer experiment is shown in figure 1. The subscript 1 is used to indicate the properties of the high-speed stream, while the subscript 2 denotes the low-speed stream properties. The velocity profile shown is that of the mean streamwise velocity.

Incompressible mixing layers have been studied experimentally since the 1940s, and a large amount of data exists for a wide range of mixing-layer attributes including growth rate, mean and fluctuating velocities, vorticity, scalar transport and mixing, as well as the effects of varying flow parameters on these attributes. While not nearly as extensive, similar experimental data exist for compressible mixing layers. One type of

---

† Present address: Department of Mechanical Engineering, Iowa State University, 3025 H. M. Black Engineering Building, Ames, IA 50011, USA.

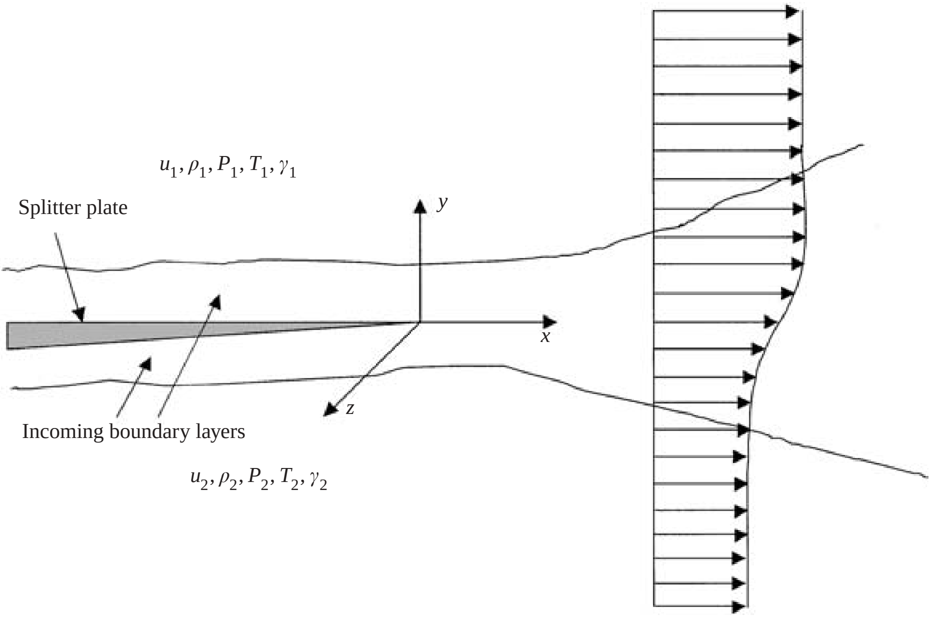

Figure 1. Diagram of a mixing layer.

measurement that is lacking for both incompressible and compressible mixing layers, however, is instantaneous planar velocity measurements.

Experiments (Johnson 1971; Brown & Roshko 1974; Bogdanoff 1984) have demonstrated that even for identical velocity and density ratios, compressible mixing layers grow more slowly than incompressible mixing layers. Further experimentation (Ikawa & Kubota 1974; Chinzei *et al.* 1986; Messersmith *et al.* 1988; Papamoschou & Roshko 1988; Elliot & Samimy 1990) has shown that it is a compressibility effect, and not just density ratio differences, between the two free streams that accounts for the lower growth rates of compressible mixing layers.

Bogdanoff (1982) introduced the convective Mach number M_c as a parameter for isolating the effects of compressibility in mixing layers. When the specific heat ratios, γ_1 and γ_2, of the two streams are equal, the convective Mach numbers of the two streams are equal, and are given by

$$M_c = \frac{u_1 - u_2}{a_1 + a_2}, \tag{1}$$

where u_1 and u_2 are the velocities of the high-speed and low-speed free streams, and a_1 and a_2 are their respective speeds of sound. For M_c less than approximately 0.6, the convective Mach number effectively collapses most of the growth rate data for compressible mixing layers to a single curve when the growth rates are normalized by the growth rate of an incompressible mixing layer with identical velocity and density ratios. The convective Mach number is not effective at collapsing data for extreme density ratios, however. At mid- to high-subsonic convective Mach numbers, the measured convective velocity begins to deviate from that predicted by analytic models (Papamoschou 1991).

In their seminal paper on incompressible mixing layers, Brown & Roshko (1974) found that large-scale two-dimensional roller structures dominate the flow field. Large-scale structures are also observed in compressible mixing layers, with the topology and behaviour of these structures highly dependent on the level of compressibility (i.e. the convective Mach number). Using a Mie scattering technique, Clemens & Mungal (1992) and Messersmith & Dutton (1996) found that at low M_c, two-dimensional Brown–Roshko-type roller structures dominate the mixing layer. However, as the convective Mach number is increased, these two-dimensional structures first become obliquely oriented in the spanwise direction, and then as M_c becomes large, the large-scale structures become highly three-dimensional, elliptically or polygonally shaped, and jagged with long filament-like braids. Unlike the roller structures found in incompressible mixing layers, these three-dimensional structures are not well organized spatially. Similar results were found by Elliott, Samimy & Arnette (1992) using filtered Rayleigh scattering and in additional experiments by Clemens & Mungal (1995) using planar laser-induced fluorescence.

Some studies of the temporal evolution of large-scale structures in compressible mixing layers have also been performed. Mahadevan & Loth (1994) used high-speed schlieren photography and laser sheet cinematography to visualize a shear layer with $M_c = 0.76$. They found that large-scale structures stretch and tilt down as they convect downstream. Elliott, Samimy & Arnette (1995) performed double-pulsed Rayleigh scattering experiments on compressible mixing layers with convective Mach numbers of 0.51 and 0.86. In their lower convective Mach number case, they observed large-scale structure behaviour similar to that seen in incompressible mixing layers. At this convective Mach number, roller-structure pairing was observed. However, at the higher convective Mach number, roller-structure pairing was not seen. Instead, the large-scale structures were observed to tear and stretch.

Velocity measurements have also been made in compressible mixing layers using laser-Doppler velocimetry (LDV). Goebel & Dutton (1991) performed velocity measurements over a range of convective Mach numbers. One of their major findings was that the transverse turbulence intensity and Reynolds shear stress decreased with increasing convective Mach number, while the streamwise turbulence intensity remained nearly constant. Similar results were obtained by Samimy & Elliott (1990), although they found that the streamwise turbulence intensity decreased somewhat with increasing M_c.

Planar velocity data for compressible mixing layers are virtually non-existent. To our knowledge, the only experiments that have been performed to date are those by Urban & Mungal (1997, 1998) and Urban, Watanabe & Mungal (1998). Their experiments consisted of PIV measurements for compressible mixing layers over a range of convective Mach numbers from 0.24 up to 0.79. They found that at low convective Mach numbers, the instantaneous vorticity fields contained discrete peaks, indicative of large-scale structures. However, as the convective Mach number was increased, the vorticity field contained thin sheets of vorticity rather than peaks, suggesting a breakdown in the large-scale structures. They also measured turbulent velocity fluctuations and Reynolds stresses and found the same compressibility effects as Goebel & Dutton (1991). The work presented here is for a different convective Mach number from the experiments of Urban *et al.* and also contains different analyses from those performed by Urban *et al.* (spatial correlations and linear stochastic estimates). In addition, data have been collected for the incompressible case for comparison purposes.

Because of the high Reynolds numbers found in compressible mixing layers, numerical studies of compressible mixing layers have thus far concentrated on linear stability analysis, and large-eddy simulations, with only a few workers attempting direct numerical simulations at low Reynolds numbers. Sandham & Reynolds (1989) performed linear stability analysis for a wide variety of mixing layers, both compressible and incompressible, and also a two-dimensional direct numerical simulation. The Reynolds numbers for these calculations were small, with $Re_{\delta_\omega} = 400$. In their stability analysis, they found that oblique waves become the dominant instabilities above $M_c = 0.6$. This could be the reason that Brown–Roshko-type structures are not seen experimentally in high convective Mach number compressible mixing layers. In their direct numerical simulation, Sandham & Reynolds found that the vortices that do develop are elongated in the streamwise direction with respect to the vortices found in incompressible mixing layers.

Other stability analyses have investigated the effect of increasing convective Mach number or introducing disturbances on mixing-layer growth rate. Ragab & Wu (1989) found that increasing convective Mach number reduces the growth rate of instability modes, and thus decreases the growth rate of a compressible mixing layer. Grosch & Jackson (1991) were able to double the growth rate of a compressible mixing layer by introducing disturbance waves. Day, Reynolds & Mansour (1998) used a linear stability analysis to study the effects of heat release, compressibility, equivalence ratio, density ratio, and velocity ratio on the growth of instabilities in chemically reacting mixing layers. Among their findings was that density ratio, convective Mach number and heat release were the most important parameters in affecting the amplification of instabilities, with equivalence ratio and velocity ratios being less important factors.

Sandham & Reynolds (1991) presented results from a true three-dimensional direct numerical simulation of a temporally evolving turbulent compressible mixing layer. They found that, as the convective Mach number is increased, the large-scale structures that develop become more three-dimensional. They also found that mixing-layer growth diminishes with increasing compressibility. They did not, however, present comparisons of turbulent velocity statistics derived from their simulations with experimental data. It is thus difficult to assess whether they truly were able to model turbulence down to the smallest scales.

Vreman, Sandham & Luo (1996) also performed direct numerical simulations for temporally evolving compressible mixing layers over a range of convective Mach numbers from 0.2 to 1.2. They, too, observed a reduction in mixing-layer growth rate with increasing compressibility. Their results suggest that reduced turbulent pressure fluctuations are responsible for the reduced growth rate seen at higher convective Mach numbers. They also found that the turbulence statistics in their simulations agreed well with experimental results.

Freund, Moin & Lele (1997) performed a direct numerical simulation of a temporally evolving annular mixing layer with convective Mach numbers ranging from 0.1 to 0.8. One of their major findings was that with increasing convective Mach number, the Reynolds stresses, with the exception of the streamwise normal stress, were suppressed. They also found a relationship between mixing-layer growth rate and pressure–strain rate correlation. Increasing convective Mach number suppresses pressure fluctuations, which suppresses the pressure–strain rate correlation, leading to reduced mixing-layer growth rate.

Because of the difficulties in performing direct numerical simulations on spatially evolving mixing layers, turbulent simulations of such mixing layers are often done using large-eddy simulation. Such a simulation was performed by Nelson & Menon (1998). They tried to match the experimental results of Samimy, Reeder & Elliott (1992) with their calculations. They found that their calculations for compressible mixing layers agreed well with experiments for low convective Mach number, but at higher convective Mach number, the results, while agreeing qualitatively with experiments, were not quantitatively correct. For example, at high convective Mach number, the calculated turbulence intensities and Reynolds shear stress profiles had the same shapes as the experimental results, but the values of the stresses were different. In fact, their results were consistent with the experimental results of Goebel & Dutton in that the streamwise turbulence intensity remained nearly constant with increasing Reynolds number.

Although a large body of experimental results exists on compressible mixing layers, instantaneous measurements of the velocity field are lacking. The work presented here is an attempt to incorporate instantaneous planar velocity measurements into the existing body of knowledge concerning compressible mixing layers. To obtain these measurements, a series of particle image velocimetry (PIV) experiments was performed. These velocity fields were then analysed to provide insight into the characteristics and behaviour of large-scale structures found in the weakly compressible mixing layer and the effects of compressibility on these structures.

The remainder of this paper is organized as follows. First, the experimental facility, including the wind tunnel and test section, is introduced. Then details of the particle image velocimetry used in the experiments, such as descriptions of the components used and the capability of the system are discussed. The experimental results from both schlieren photography and particle image velocimetry are then presented and discussed. This discussion includes how the present findings fit into the context of existing experimental and numerical results. Finally, the conclusions drawn from this experimental study are summarized.

2. Experimental facilities and equipment

2.1. *Wind tunnel*

The flow facility designed for these experiments is of the blowdown-type. High-pressure air is provided by an Ingersoll-Rand compressor that supplies 1200 SCFM at an operating pressure of 115 p.s.i.g. The high-pressure air from this compressor first flows into several interconnected pressure vessels with a total volume of 150 m^3, collectively known as the tank farm. The air from the tank farm enters the laboratory through a 6 in diameter pipe. The flow to the test section is regulated using a 6 in Fisher control valve; after passing through the control valve, the air enters the facility stagnation chamber.

Figure 2 shows the test section used in the mixing-layer experiments. Two 3 in diameter pipes supply air to the top (high-speed) and bottom (low-speed) streams. The pipe to the bottom stream is fitted with a globe valve to allow for throttling. Each of the two streams is conditioned by a combination of three screens and one honeycomb insert to provide uniform flow and reduce the free-stream turbulence intensity. The high-speed stream contains a converging–diverging nozzle designed for Mach 2 flow. The low-speed stream contains a converging nozzle with a 6 : 1 area contraction ratio. The two streams come together at the tip of the splitter plate. The splitter plate has been machined such that it is only a few hundredths of a millimetre thick at its tip with a 3° included angle between the two streams. The test section is 63.5 mm high, 102 mm wide and 356 mm long. Also, the test section has been designed with windows on all four walls, thus providing optical access to all sides of the test section.

2.2. *Seeding*

For the PIV experiments, the flow must be seeded with particles that are small enough to accurately follow the flow. The seeding used in these experiments was titanium dioxide ($\mathrm{TiO_2}$) particles with an average diameter of 0.4 μm, as measured

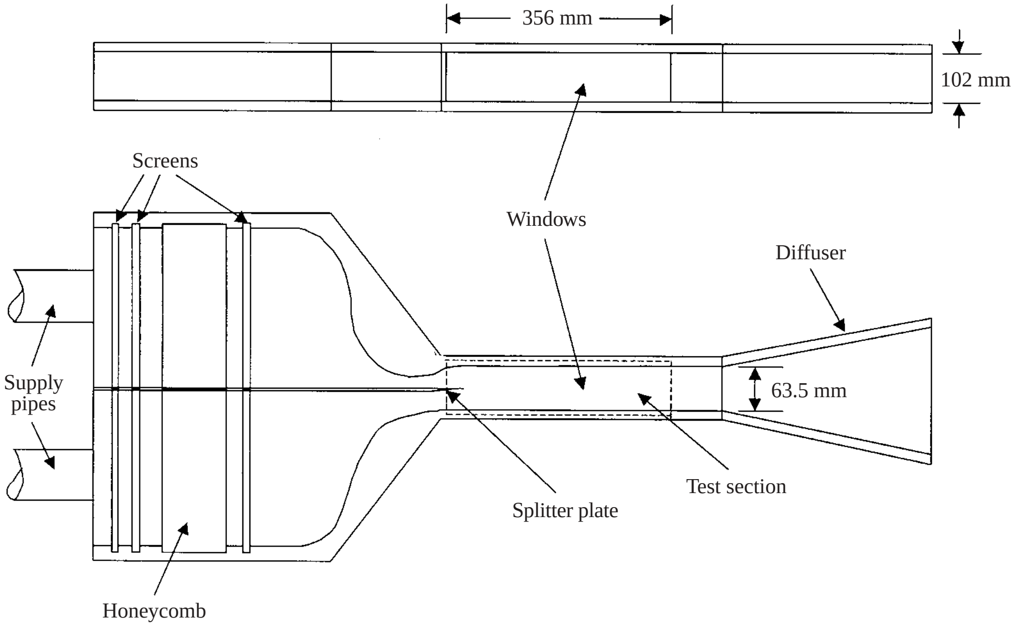

Figure 2. Mixing-layer facility schematic.

by Bloomberg (1989). An analysis of the dynamics of particles in a compressible mixing layer was performed by Samimy & Lele (1991), and their results were used to determine the effectiveness of the seed particles used in these weakly compressible mixing-layer experiments. For the current experiments, the particle Stokes number had a value of $\tau = 0.041$. In their analysis, Samimy & Lele found that for $\tau < 0.05$, the error in velocity measurement owing to particle slip was negligible. Thus, for the present experiments, the titanium dioxide particles should closely follow the flow.

Obtaining sufficient seed particle density and uniformity was very challenging in performing these experiments. Initially, we injected the seed particles into each of the free streams using tubes, but we found the seed uniformity using this injection scheme to be unacceptable. Instead, we found that we achieved better seeding uniformity by injecting the seed particles into the stagnation chamber. Using this technique, we were eventually able to achieve a high enough seed density such that there were at least 5 particle images per interrogation spot (and usually, a great deal more), resulting in a very high interrogation success rate.

2.3. *Particle image velocimetry system*

The particle image velocimeter used in the current experiments consists of separate acquisition and interrogation systems. The acquisition system includes the lasers, beam-shaping optics, and 35 mm camera used to obtain the particle image photographs of the flow field. The interrogation system is comprised of the CCD camera, light source, positioning system, controlling computer, and digital signal processors necessary to calculate vector fields from the PIV photographs.

The acquisition system used in these experiments was designed explicitly for high-speed flows, and therefore contains several features that are different from those found in a system used for low-speed flows. The lasers used in the acquisition system are a pair of Continuum YG681C-10 Nd:YAG lasers that emit 532 nm light at a pulse repetition rate of 10 Hz. The high pulse energy (550 mJ per pulse) of these lasers is necessary to illuminate the small particles used in these experiments. The short duration (6–8 ns) of the laser pulses is desirable because this eliminates any blurring of the particle images due to motion during the pulse.

The PIV photographs were obtained using a Canon EOS 35 mm film camera. The camera was fitted with a 100 mm focal length lens. This lens has a maximum $f\#$ of 2.8, but for the weakly compressible mixing-layer experiments, the lens aperture was partially closed, resulting in $f\# = 6.7$.

A critical factor in the acquisition of the PIV photographs is accurate timing of the laser pulses. The timing of the acquisition system was controlled by a Stanford Research Systems DG535 digital delay pulse generator. A small uncertainty in the time separation of the laser pulses is present owing to the pulse jitter of each laser, which is approximately 1 ns. The DG535 has a timing resolution of 5 ps, but this is much smaller than the pulse jitter and can thus be ignored. For the weakly compressible mixing-layer experiments, a time separation of 400 ns between laser pulses was used, resulting in an experimental uncertainty due to pulse jitter of $\pm 0.25\%$.

The interrogation system used to compute the velocity vector fields from the PIV photographs is controlled by a 90 MHz Pentium computer. The photographic negative is placed in a glass sandwich and small regions of the photograph are imaged onto a CCD camera. A two-axis positioner controls the location of the negative, allowing different regions of the recorded flow field to be imaged. A frame grabber residing within the host computer digitizes the image, and the digitized image is then sent to a digital signal processing (DSP) board containing two Texas Instruments TMS320C44 processors. The DSP board performs a cross-correlation analysis on the digitized image to find the velocity vector at each interrogation spot location. The system is capable of computing about 6 vectors per second.

The experimental uncertainty of the PIV measurements must be addressed. In a detailed study of interrogation accuracy, Prasad *et al.* (1988) found that when particle images are well resolved during digitization, the uncertainty of the measurement is equal to roughly one-tenth of the particle image diameter. This uncertainty is due to the error associated with locating the particle location to subpixel resolution using a centroidal method. A particle image is considered to be well resolved when the ratio of the particle image diameter to the size of the CCD pixel when projected back onto a photograph is $d_{image}/d_{pixel} = 4$. In the experiments presented here, the particle diffraction-limited spot size is 40 μm. Each 128×128 pixel interrogation spot is $1200\,\mu\text{m} \times 1200\,\mu\text{m}$, thus $d_{pixel} = 9.38$ μm. It follows then that $d_{image}/d_{pixel} = 4.3$, so that the images are well resolved. Approximating the measurement uncertainty as one-tenth of the particle image diameter yields an uncertainty of 4 μm. In the current experiments, the bottom free-stream velocity corresponds to a displacement of 113 μm and the top free-stream velocity corresponds to a displacement of 216 μm. Thus, for these experiments, the measurement uncertainty is $\pm 3.5\%$ for the bottom free stream and $\pm 1.9\%$ for the top free stream.

3. Results and discussion

For the weakly compressible mixing-layer experiments, the top and bottom free stream velocities were set at 510 m s^{-1} and 270 m s^{-1}, respectively. This corresponds to a velocity ratio of $r = u_2/u_1 = 0.53$. Because static temperature is dependent on Mach number in homenergetic flow, the two free streams have different static temperatures, and thus different densities. For the flow conditions used in these experiments, the density ratio was $s = \rho_2/\rho_1 = 0.67$.

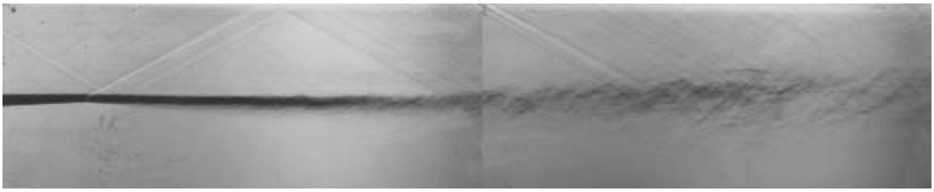

Figure 3. Schlieren photograph of the weakly compressible mixing layer.

As described earlier, the parameter that is used to quantify compressibility effects in mixing layers is the convective Mach number. For these experiments, the convective Mach number is 0.38. Compressibility effects begin at approximately $M_c = 0.3$, but do not become dominant until around $M_c = 0.6$ (Dutton 1997). Thus, in these experiments, there should be some compressibility effects present, but these effects should be rather weak. Even so, the planar velocity measurements presented and discussed below show some significant differences from corresponding results for incompressible mixing layers.

3.1. *Schlieren photography*

A composite schlieren photograph of the weakly compressible mixing layer is shown in figure 3. Little evidence of large-scale turbulent structure can be seen in the photograph until the downstream half of the flow field. While some braid-like structure is present in this region, dominant rounded Brown–Roshko rollers are clearly not evident.

Among the other features visible in this figure are weak disturbance waves in the top (supersonic) free stream. There is a disturbance wave emanating from a point on the top wall upstream of the tip of the splitter plate that then propagates downstream. This wave is caused by the seam where the top window frame fits into the top wall of the test section. Another disturbance, a weak oblique shock wave, is formed at the tip of the splitter plate, and it also propagates downstream, reflecting off both the top wall of the tunnel and the mixing layer. This oblique shock wave is caused by the slight mismatch in static pressure at the splitter plate tip (which can vary slightly with time) and by the 3° angle of convergence of the two free streams at the tip, as well as the confinement effects on the supersonic free stream owing to the presence of the top wall of the wind tunnel. A final disturbance is observed originating just upstream of the location where the two photographs are spliced together. This is formed at the location where the top window is epoxied into the window frame. Since there is no perceptible turning of the mixing layer at the locations where all these disturbance waves intercept it, each of the waves is deemed to be weak. However, the intermittent nature of the wave generated at the splitter plate tip does influence the velocity measurements in the top free stream to a small extent, as will be shown shortly. The intermittent nature of the waves is a possible concern, because the waves could affect the nature of both the large-scale turbulent structures and entrainment. However, because the measured mixing-layer growth rate agrees well with previous experiments, we believe that such effects are small.

An estimate of mixing-layer growth is determined from the schlieren photograph. First, an estimate of the ratio of the visual thickness of the mixing layer, as measured from the schlieren photograph, to the vorticity thickness of the weakly compressible mixing layer, as determined using PIV measurements, must be made. At the location where the PIV photographs were obtained, the vorticity thickness of the mixing layer was found to be 13.5 mm, and the visual mixing-layer thickness in the schlieren photograph is 17 mm, thus, $\delta_\omega/\delta_{vis} = 0.79$. This ratio is assumed to be constant over the entire range of the schlieren photograph. The growth rate for the weakly compressible mixing layer is then estimated from the schlieren photograph as $\mathrm{d}\delta_\omega/\mathrm{d}x = 0.038$. According to Papamoschou & Roshko (1988) and Dutton (1997), the expected vorticity-thickness growth rate for an incompressible mixing layer can be calculated using

$$\left(\frac{\mathrm{d}\delta_\omega}{\mathrm{d}x}\right)_{\text{incompressible}} = 0.165\frac{(1-r)(1+s)^{1/2}}{2(1+rs)^{1/2}}, \tag{2}$$

which, for the present mixing-layer experiment, yields $\mathrm{d}\delta_\omega/\mathrm{d}x = 0.049$. Thus, the growth rate of the current mixing layer is only 78% of the growth rate for an incompressible mixing layer with identical velocity and density ratios. This growth-rate reduction agrees well with previous experimental results for convective Mach numbers near the current 0.38 value (Dutton 1997).

3.2. *Particle image velocimetry measurements*

3.2.1. *Measurement parameters*

An ensemble of 37 PIV velocity vector fields was obtained at a location 220 mm downstream of the tip of the splitter plate. The size of this ensemble was limited because of the difficulty of obtaining uniform and sufficient seed particle density to obtain successful PIV vector fields in high-speed flows. An interrogation spot size of 1.2 mm was used, and with 50% overlap between adjacent interrogation spots, this results in a spatial resolution of 0.6 mm in both the x- and y-directions. The vector fields presented here measure 70×70 vectors.

As mentioned previously, the vorticity thickness of the weakly compressible mixing layer at the measurement location is 13.5 mm. Thus, there are 22.5 velocity vectors measured across the thickness of the mixing layer, providing good spatial resolution of the large-scale turbulence. At this downstream location, the Reynolds numbers based on distance from the splitter-plate tip and local mixing-layer vorticity thickness are $Re_x = 3.7 \times 10^6$ and $Re_{\delta_\omega} = 1.8 \times 10^5$, respectively. Goebel & Dutton (1991) found in their compressible mixing-layer experiments that self-similarity was achieved for $Re_{\delta_\omega} > 10^5$. Thus, it is safe to assume that in the current experiment, the mixing layer is fully developed with respect to both mean and turbulence quantities.

3.2.2. *Instantaneous velocity field results*

A typical instantaneous velocity field for the weakly compressible mixing layer is shown in figure 4. In this vector field and in all vector fields presented herein, the mean free-stream velocity of 390 m s^{-1}, which approximates the expected convective velocity, has been subtracted from each of the vectors to make the large-scale structures more apparent. The coordinate system used in the vector plots is such that the tip of the splitter plate is at (0,0). In figure 4, two large Brown–Roshko-like roller structures can be seen near the left and right centre of the image with a braid region between them. In this image and other images of the mixing layer, the presence of three-dimensionality and small-scale structures can make identification of large-scale structures difficult.

Evidence of Brown–Roshko-like rollers structures in a compressible mixing layer has been reported before. In direct numerical simulations by Sandham & Reynolds (1991) of a temporally evolving compressible mixing layer with $M_c = 0.4$ (very close to that of the present experiment), roller structures were very clearly observed as well as the braid regions between them. Of course, their simulations were for $Re_{\delta_\omega} = 400$ compared to $Re_{\delta_\omega} = 1.8 \times 10^5$ in the present experiment, so the simulation did

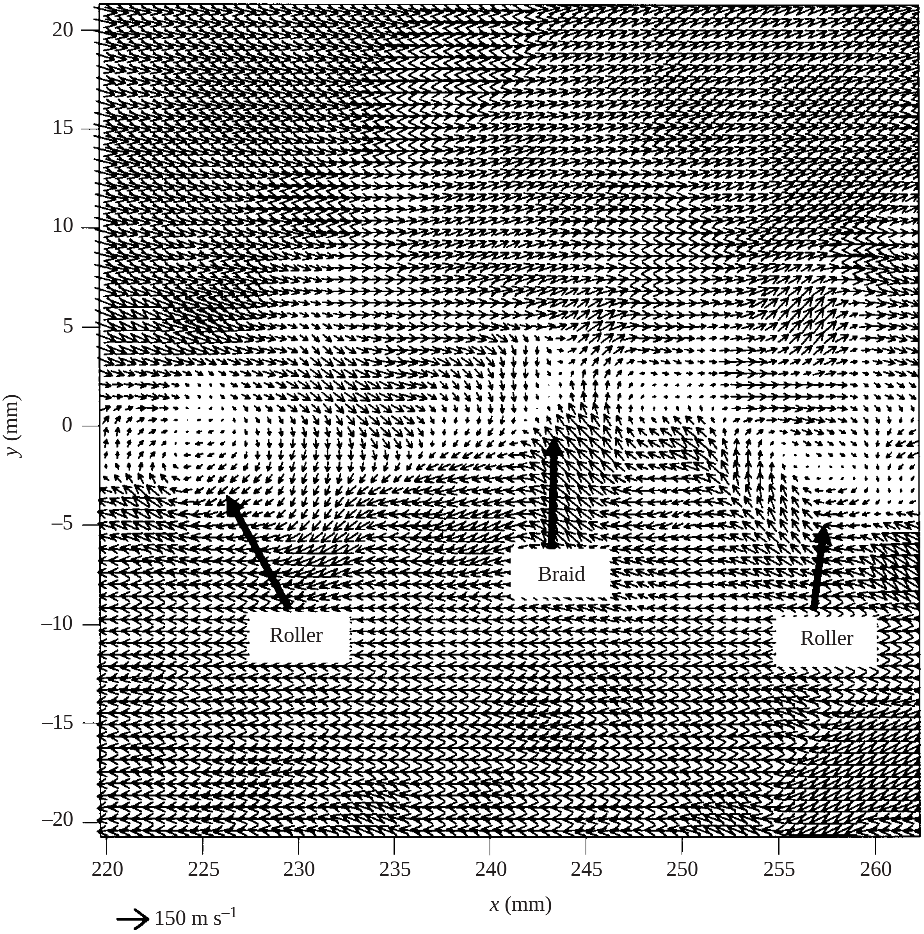

FIGURE 4. A typical weakly compressible mixing-layer vector field. This velocity field is in the first regime.

not contain the small-scale structure of the PIV vector fields, but the large-scale structures were visible nevertheless. Similarly, pressure correlation measurements by Samimy *et al.* (1992) indicated the presence of structures at $M_c = 0.51$ similar to those in the incompressible case, only less organized.

Clemens & Mungal (1995) also observed the presence of Brown–Roshko-like structures in their planar Mie scattering experiments. They found evidence of very persistent Brown–Roshko structures up to $M_c = 0.28$, and these structures were still evident at $M_c = 0.42$, although they were much more disorganized. At $M_c = 0.62$, they reported that the Brown–Roshko structures were no longer identifiable.

Another feature of the flow field that can be observed in figure 4 is the presence of a weak oblique shock wave in the top free stream. On the left-hand side of the vector field, the top free stream vectors have a small downward velocity component. However, a weak oblique shock wave can be seen beginning near $x = 228$ mm, $y = 6$ mm and extending diagonally up into the top free stream. This shock wave has the effect of slightly turning the flow such that the velocity vectors in the top free stream to the right of the shock wave have a small upward velocity component. The shock wave would hardly be visible at all if the large convective velocity had not been

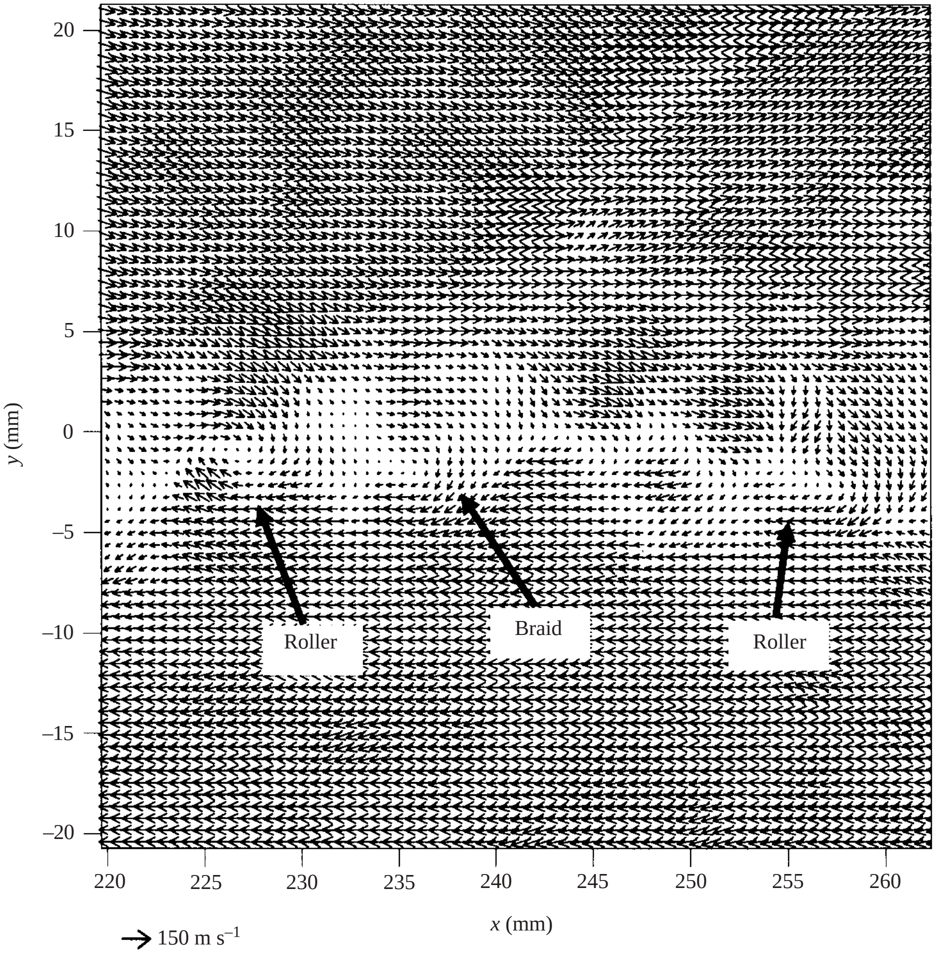

FIGURE 5. A velocity vector field for the weakly compressible mixing layer in the second regime.

subtracted away. The shock wave is not present in all of the vector fields, and when it is present, it has varying strength. Because of the intermittency of its occurrence, this shock wave is thought to be the result of small intermittent pressure mismatches at the splitter-plate tip. When the pressures are perfectly matched, there is no shock wave, but any variation between the pressures of the two free streams will cause a weak shock wave or expansion fan to appear. The effect of these weak waves in the high-speed free stream will be discussed again later.

Although figure 4 is a typical result for the velocity vector field, it is in no way representative of all the vector fields. Indeed, the individual velocity fields comprising the ensemble fall predominantly into three different regimes. The first regime is typified by the vector field in figure 4, and is characterized by large-scale Brown–Roshko-like roller structures similar to those observed in incompressible mixing layers, except with more small-scale structures superimposed on the rollers.

The second regime contains vector fields similar to that shown in figure 5. This velocity field has a number of smaller roller structures, some of which are moving at different convective velocities to the others. For example, there is one roller structure

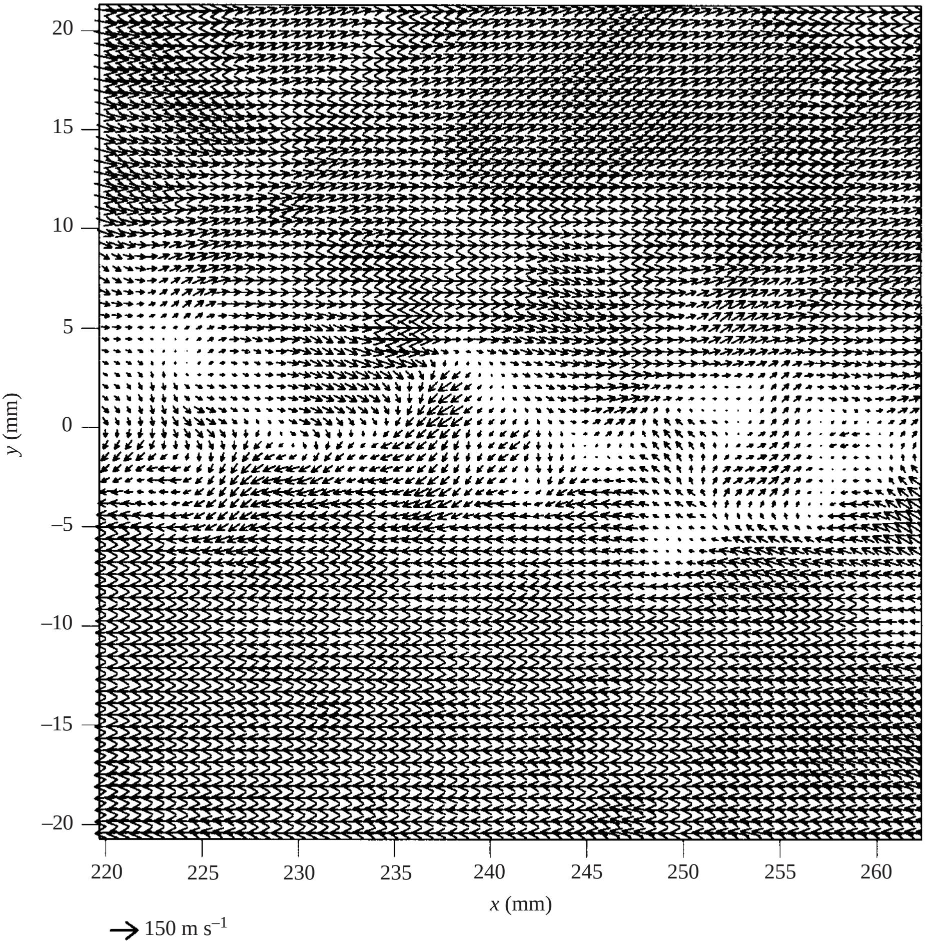

FIGURE 6. A velocity vector field for the weakly compressible mixing layer in the third regime.

at (226 mm, −1 mm), another at (236 mm, −2 mm), a third at (250 mm, −2 mm) and a fourth at (255 mm, −3 mm). The second, third and fourth roller structures are not as visible as the first, most probably because they are moving at a different convective velocity to the first, so that the circulation pattern about these structures is not as readily apparent. Also, each of these structures is smaller than the two large structures present in figure 4. This observation of a second flow regime is in agreement with the results of Clemens & Mungal (1995), who observed that at $M_c = 0.42$, large-scale structures, although present, were disorganized and intermittent.

An example of a velocity vector field in the third regime is presented in figure 6. This vector field contains little evidence of large-scale structures, and instead appears to be dominated by small-scale structures. There may be a small roller structure located near (230 mm, −2 mm), although it is apparently moving at a convective velocity different from 390 m s^{-1}. In addition, there appears to be a stagnation region at (245 mm, −2 mm), but other than these two features, there are no readily discernible large structures. The three flow regimes observed in these experiments are consistent with previous flow-visualizations (Messersmith & Dutton 1996; Clemens & Mungal, 1995; Elliott *et al.* 1995), where large variability in flow structure was seen in the image ensembles for compressible mixing layers.

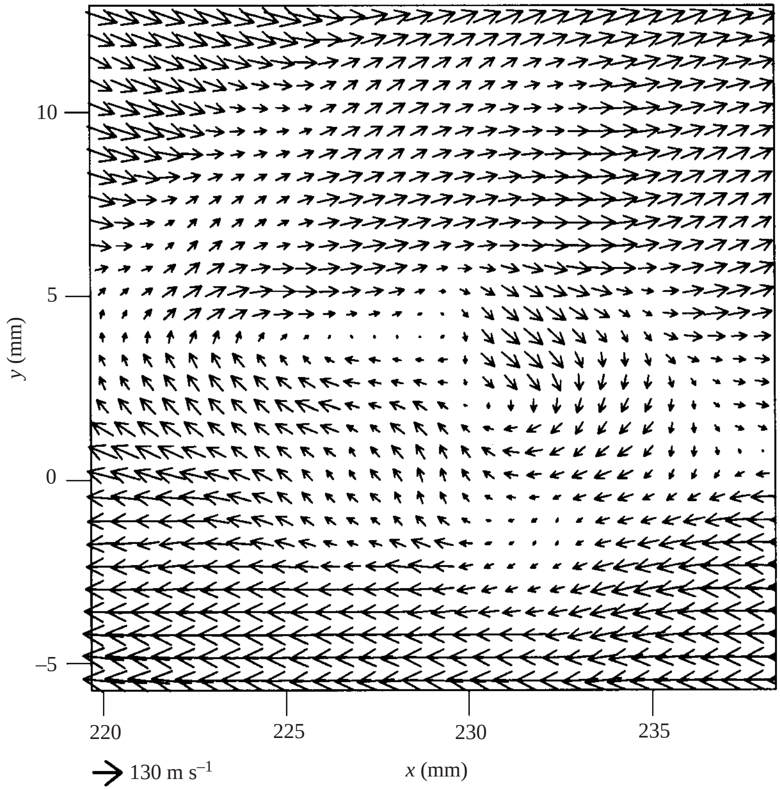

FIGURE 7. Close-up of the interaction of two roller structures showing a possible pairing.

3.2.3. *Structure pairing*

In incompressible mixing layers, one mechanism for mixing-layer growth is the pairing of two or more large-scale structures into a larger structure (Browand & Latigo 1979). This pairing process has also been observed in the current weakly compressible mixing layer. One example of a possible roller pairing is presented in figure 7. In this figure, there is a horizontally oriented elliptical roller structure centred at (229 mm, 4 mm) with a smaller circular roller structure to its lower right-hand side. These two roller structures appear to have progressed in the pairing process, as the stagnation region between them has completely disappeared. There is also a large region of circulation around both of the rollers, indicating that the two structures have begun to act as a single structure.

Figure 8 shows another pair of roller structures in the process of pairing to form a larger structure. These two structures have nearly completed the pairing process. There is a large circular roller structure centred at (230 mm, −1 mm), and to its lower right-hand side the remnants of a smaller structure can be seen. This smaller structure appears as a small bump on the larger roller structure and is somewhat difficult to discern.

Each of the velocity fields in the ensemble that depict roller pairing are similar to those in figures 7 and 8 in that the trailing roller is always at an angle of approximately 45° and above the leading roller. The two interacting roller structures are never observed to be oriented with one on top of the other. Although the ensemble size is certainly small, this might suggest that for the weakly compressible case, instead

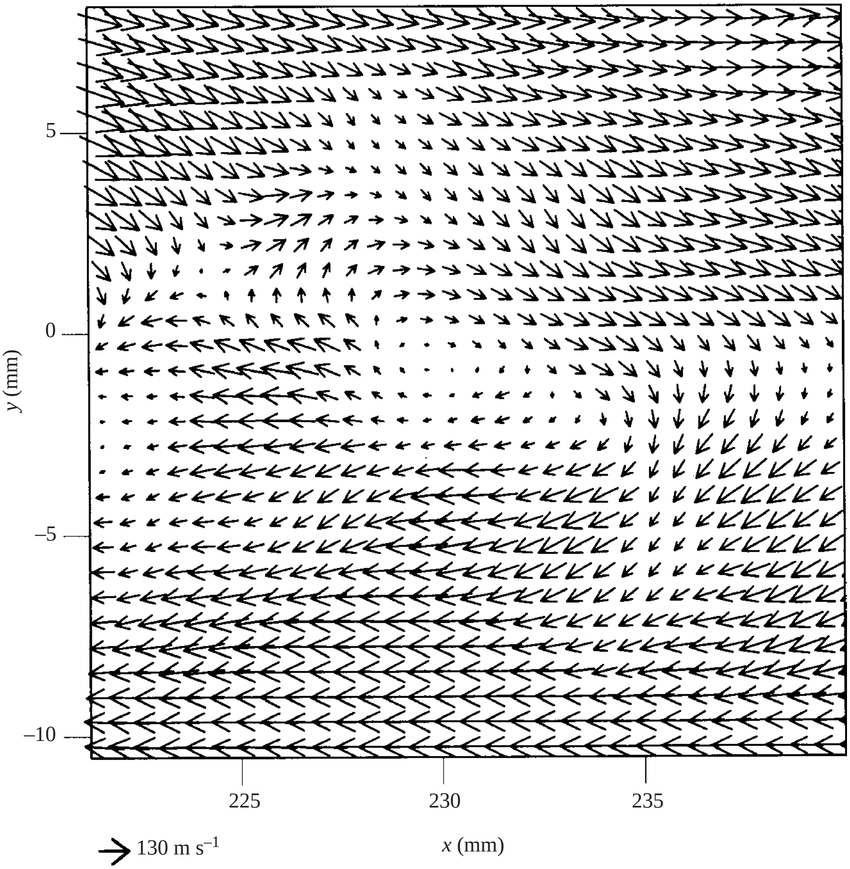

FIGURE 8. Close-up of the interaction of two roller structures showing late stages of a possible pairing.

of the 'rotational pairing' that is observed in incompressible mixing layers (Browand & Latigo 1979), the two rollers merge by a 'slapping' mechanism in which there is little rotation of the structures about each other. This is consistent with the Mie scattering cinematography results of Mahadevan & Loth (1994) for compressible mixing layers.

3.2.4. *Mean velocities and reynolds stresses*

Although the ensemble of 37 velocity vector fields is relatively small, a method was devised to obtain more reliable velocity statistics for the PIV vector fields. Mean velocity and Reynolds stress profiles were created by collapsing the 70 columns of velocity vectors in each of the fields into a single column. Some error is introduced in doing this because the mixing layer grows as it moves downstream, and thus it is thicker on the right-hand edge of the vector field than on the left. The growth rate is small, however, and thus, its effect is believed to be negligible. Recall from the schlieren results that $d\delta_\omega/dx = 0.038$. This results in the vorticity thickness of the mixing layer increasing by about 10% from the left-hand side of the velocity vector field to the right. Collapsing the velocity field columns results in an ensemble of 2590 realizations at each transverse location, an ensemble large enough to provide reliable velocity statistics. These are not 2590 completely independent realizations, however, as multiple realizations are obtained from a single velocity vector field; but

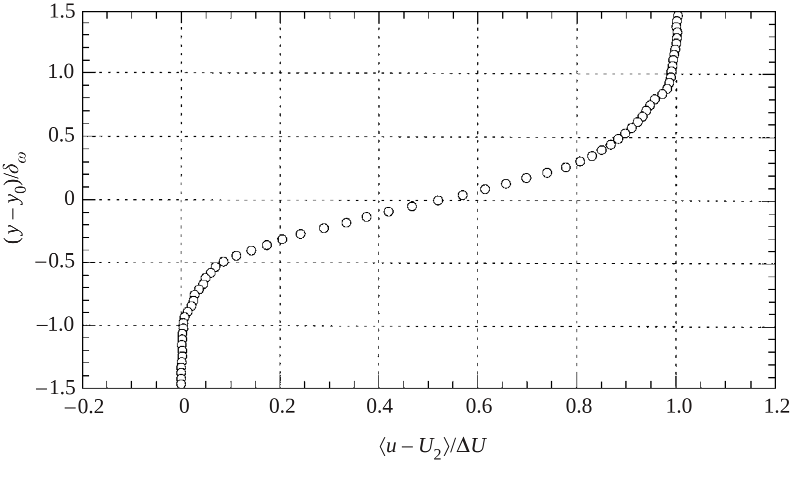

FIGURE 9. Mean u-velocity profile as measured by PIV.

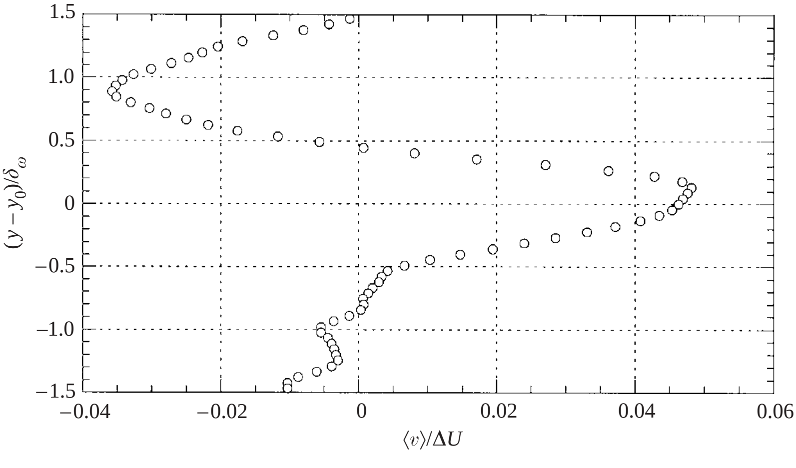

FIGURE 10. Mean v-velocity profile as measured by PIV.

rather represent velocity measurements obtained at high-data density over a relatively limited number of turbulent structures.

The mean u-velocity profile as measured by PIV is shown in figure 9. It has the same error-function-type shape as the fully developed mean u-velocity profile for the incompressible mixing layer (Brown & Roshko 1974). The y-axis has been normalized by the vorticity thickness, a procedure that will be followed in all of the profile plots presented. Also, in this figure and in the other statistical profiles to follow, y_0 is defined as the point where the mean u-velocity is equal to the average of the top and bottom free-stream velocities.

The mean v-velocity profile is shown in figure 10. This velocity profile has both a negative peak in the upper portion of the mixing layer and a positive peak in the lower portion, indicating entrainment of fluid into the mixing layer from each of the free streams. In addition, the peaks are skewed toward the high-speed stream. This phenomenon was also observed in similar PIV experiments performed for an incompressible mixing layer (Olsen 1999; Olsen & Dutton 2002), but for the weakly

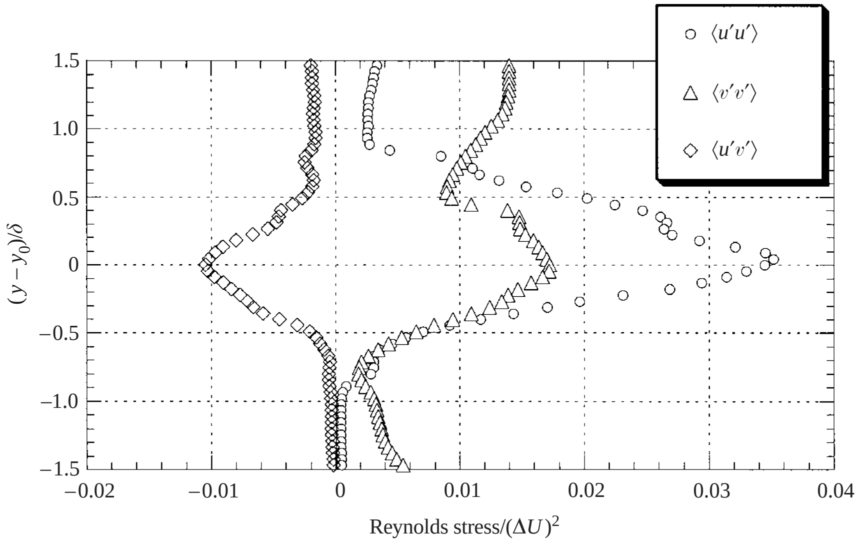

FIGURE 11. Reynolds stress profiles as measured by PIV.

compressible case, the effect is much more pronounced. Another point to note is that the magnitudes of the v-velocity are small compared to those for the incompressible mixing layer. Since the mean v-velocity is directly related to the entrainment of fluid from each of the free streams, the reduction of the mean v-velocity with increasing compressibility demonstrates a major effect of compressibility on mixing layers, namely that mixing layer growth rate decreases with increasing convective Mach number. This effect has been observed both experimentally (Elliott & Samimy 1990; Goebel & Dutton 1991) and computationally (Sandham & Reynolds 1989, 1991; Nelson & Menon 1998) and is confirmed here.

The Reynolds stress profiles are shown in Figure 11. The Reynolds normal stresses, $\langle u'u'\rangle$ and $\langle v'v'\rangle$, are seen to peak near the centre of the mixing layer and decay moving away from the centre of the mixing layer. Although $\langle v'v'\rangle$ increases again in the top free stream, this is not caused by increased turbulence in the top free stream, but is instead a result of the slight turning of the velocity vectors in those vector fields that contain the oblique shock wave discussed earlier. In each of the individual vector fields, there is low turbulence in the top free stream. However, the v-velocity in the top free stream varies from vector to vector depending on whether or not the oblique shock wave is present, and this creates ‘false turbulence’. The Reynolds shear stress $\langle u'v'\rangle$ also peaks at the centre of the mixing layer and decays moving towards the free streams and has the expected negative values.

In previous PIV measurements of an incompressible mixing layer (Olsen & Dutton 2002), which were performed at a Reynolds number of $Re_{\delta_\omega} = 1.1 \times 10^4$, the peak values of $\langle u'u'\rangle/(\Delta U)^2$, $\langle v'v'\rangle/(\Delta U)^2$, and $\langle u'v'\rangle/(\Delta U)^2$ were 0.032, 0.026 and −0.010, respectively. For the current weakly compressible mixing layer, these same quantities have peak values of 0.036, 0.017 and −0.010. This suppression of $\langle v'v'\rangle$ with increasing compressibility is consistent with previous compressible mixing-layer research (Goebel & Dutton 1991). Generally, turbulence intensities (square root of normal stresses) are presented in the literature and not the Reynolds normal stresses. The peak values of the turbulence intensities and also the Reynolds shear stress are shown in table 1, along with the results from previous experiments for convective Mach numbers near

Experiment	Re_x	Re_{δ_ω}	M_c	$\langle u' \rangle/\Delta U$	$\langle v' \rangle/\Delta U$	$\lvert\langle u'v' \rangle/(\Delta U)^2\rvert$
Present	1.8×10^5	1.1×10^4	0.02	0.18	0.16	0.010
	3.7×10^6	1.8×10^5	0.38	0.19	0.13	0.010
Goebel & Dutton (1991)	3.1×10^6	7.0×10^4	0.20	0.22	0.15	0.017
	4.8×10^6	1.3×10^5	0.46	0.17	0.10	0.0086
Urban & Mungal (1998)	3.4×10^6	1.5×10^5	0.25	0.17	0.13	0.012
	5.3×10^6	4.0×10^5	0.63	0.16	0.09	0.008
Samimy & Elliott (1990)	–	–	0.51	0.16	0.11	0.008
	–	–	0.64	0.15	0.10	0.008

TABLE 1. Comparison of turbulence quantities for compressible mixing-layer experiments.

the current value of 0.38. Although none of the previous experiments were performed at exactly the same M_c as the present experiment, the current results do seem to agree with the previous results. However, it is difficult to draw definitive conclusions from the present experiment because the convective Mach number is substantially lower than those reported by previous researchers.

3.2.5. *Vorticity and strain rate*

One major advantage of PIV over other velocimetry techniques is that the instantaneous nature of the PIV planar velocity fields allows for the calculation of instantaneous derivative quantities such as vorticity and strain rate. Figure 12 is the instantaneous vorticity field derived from the velocity field shown in figure 4. PIV results for an incompressible mixing layer (Olsen & Dutton 2002) revealed that, in general, negative peaks in vorticity correspond to the centres of roller structures. There are several negative peaks of vorticity in figure 12, and the two largest of these do seem to correspond to the roller structures seen in the velocity field. There are other smaller vorticity peaks in figure 12, and these are due to the presence of small-scale turbulence in the mixing layer. There is also non-zero vorticity in each of the free streams owing to small-scale turbulent structures located there. It is important that roller structures correspond to negative peaks in vorticity in that negative peaks in vorticity can be used to define an event based upon which the linear stochastic estimate of a roller structure can be found.

The instantaneous shear strain rate field for the velocity field shown in figure 4 is presented in figure 13. The incompressible mixing-layer PIV experiments indicated that, in general, negative peaks in strain rate corresponded to the location of braids. Such a negative peak in strain does occur directly below what visually appears to be a braid in the velocity vector field of figure 13. The fact that the two do not coincide is most probably a consequence of the braid moving at a convective velocity different to the value subtracted from the vector field. There are also positive peaks of shear strain in the mixing layer, and these generally correspond to the roller structures. Some non-zero strain peaks are seen both in the top and bottom free streams, a consequence once again of free-stream turbulence. With it having been determined that negative peaks in shear strain correspond to braid structures, this information can be used in defining an event to determine the linear stochastic estimate of a braid.

3.2.6. *Spatial correlations*

Because of the instantaneous two-dimensional nature of the PIV vector fields, spatial velocity fluctuation correlations can also be determined easily. First, spatial

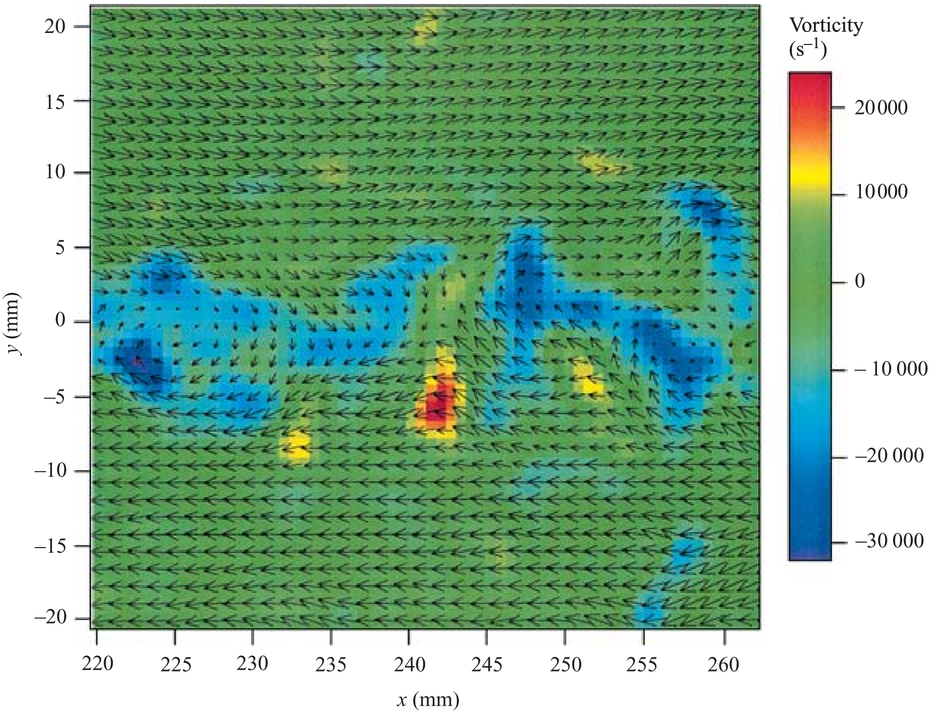

FIGURE 12. Instantaneous vorticity field for the weakly compressible mixing layer.

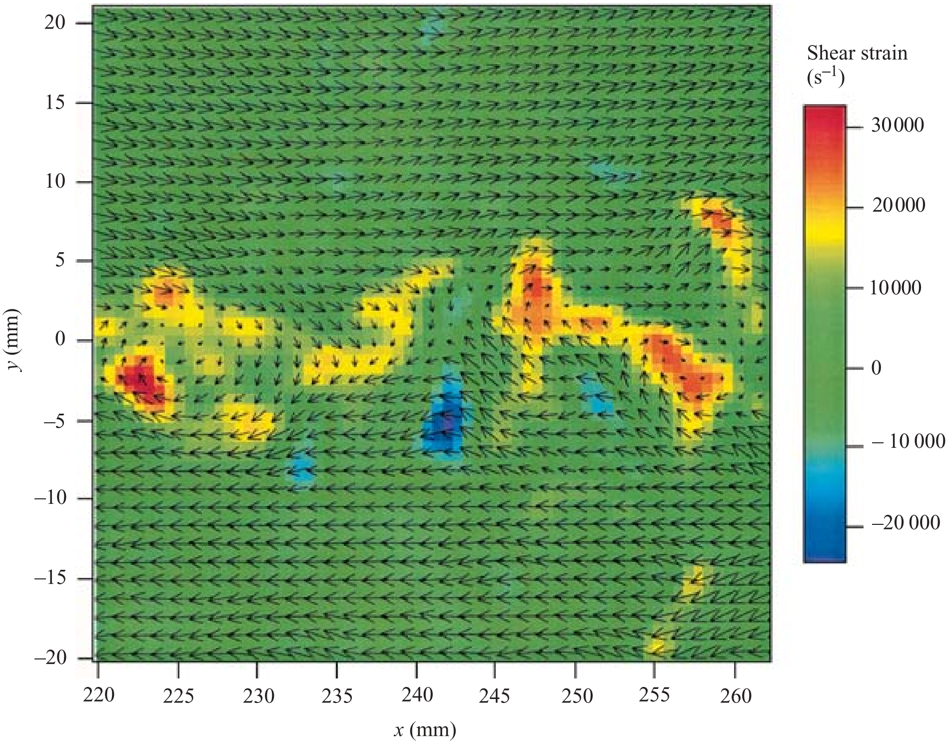

FIGURE 13. Instantaneous shear strain rate field for the weakly compressible mixing layer.

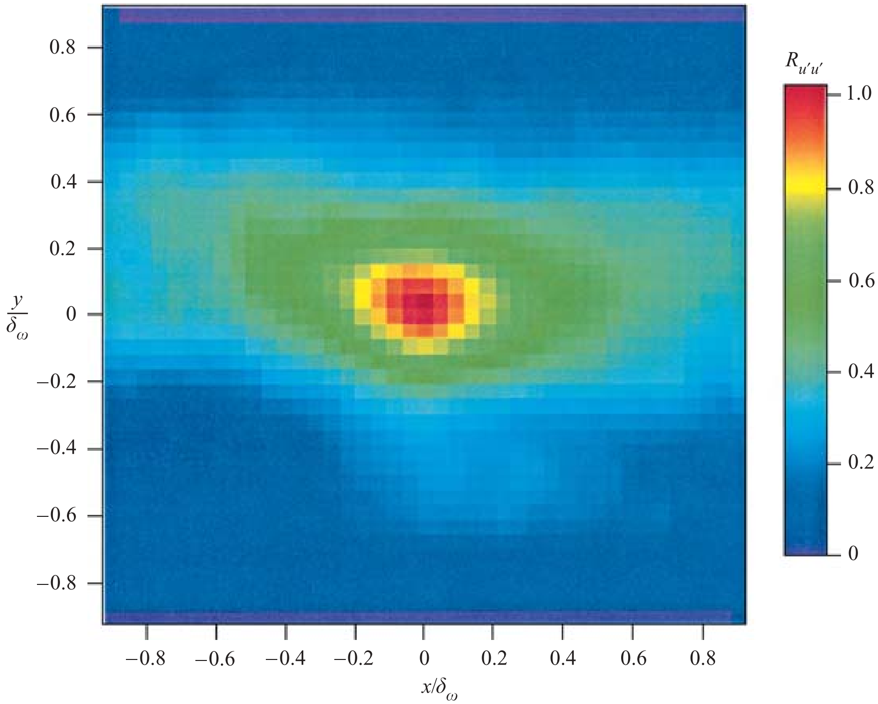

FIGURE 14. The spatial correlation $R_{u'u'}$ for the weakly compressible mixing layer.

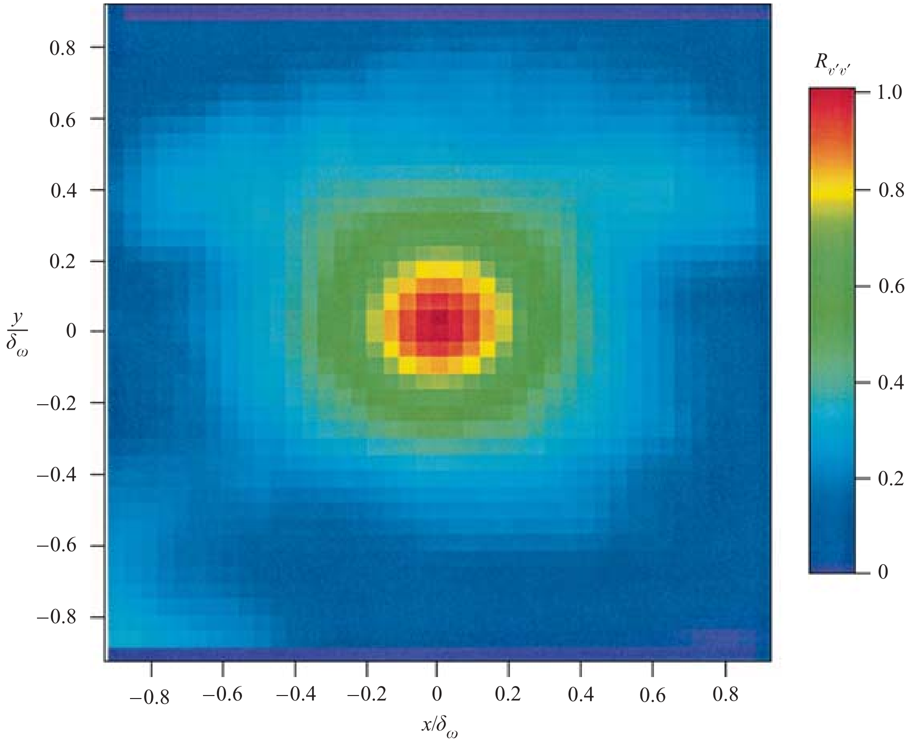

FIGURE 15. The spatial correlation $R_{v'v'}$ for the weakly compressible mixing layer.

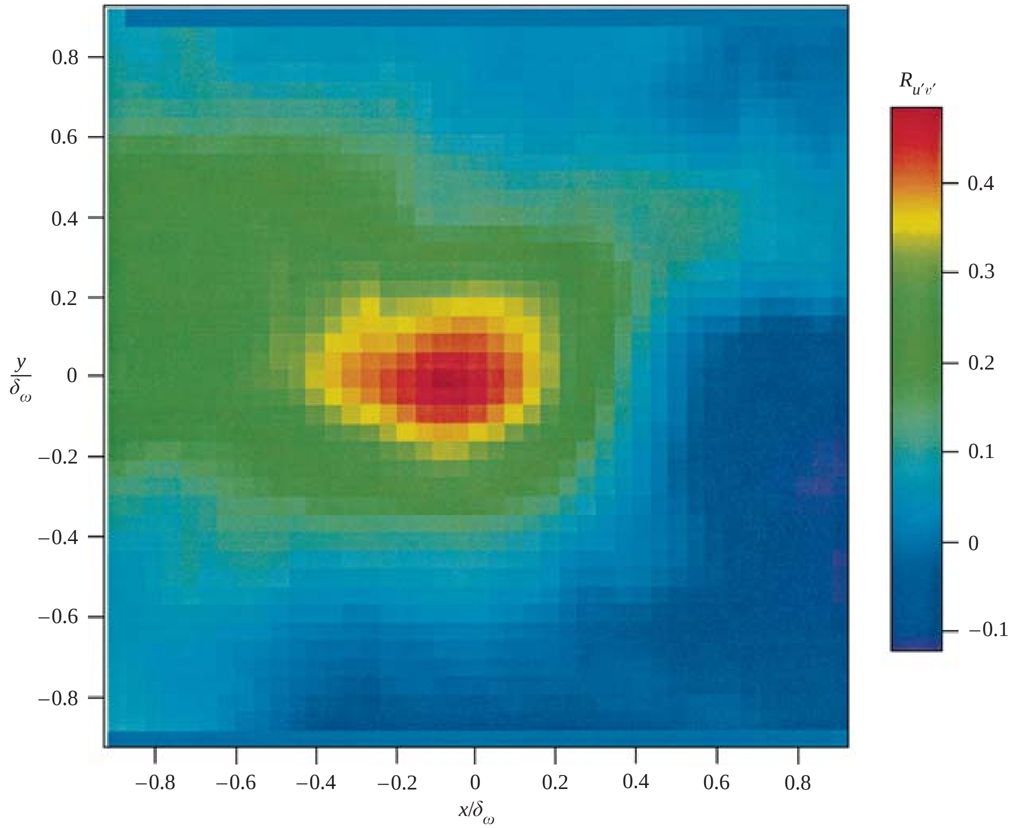

FIGURE 16. The spatial correlation $R_{u'v'}$ for the weakly compressible mixing layer.

correlations were calculated using thirteen basis points in each vector field. These basis points were all on the transverse centreline of the mixing layer (where the centreline is defined by those points where the velocity is the mean of the two free streams) and were equally spaced in the x-direction. For each of these points, the spatial correlation was calculated as

$$\langle u_i'(x,y)u_j'(x,y;X,Y)\rangle = u_i'(x,y)u_j'(x+X,y+Y), \tag{3}$$

where (x, y) are the coordinates of the basis point (the point about which the spatial correlation is calculated) and (X, Y) are the displacements from the basis points. For these calculations, the area over which the spatial correlation is calculated is a square of 41 vectors by 41 vectors centred on the basis point. The ensemble average of the spatial correlations for all of the basis points (481 realizations in all) was then calculated and normalized by $\sqrt{\langle u_i'(x,y)\rangle\langle u_j'(x,y)\rangle}$ resulting in

$$R_{u_i'u_j'}(x,y;X,Y) = \frac{\langle u_i'(x,y)u_j'(x,y;X,Y)\rangle}{\sqrt{\langle u_i'(x,y)\rangle\langle u_j'(x,y)\rangle}}. \tag{4}$$

The spatial correlation $R_{u'u'}$ for the weakly compressible mixing layer is shown in figure 14. The corresponding spatial correlation for an incompressible mixing layer has been previously calculated and presented (Olsen & Dutton 2002). In both the incompressible and compressible cases, the correlation is a horizontally oriented ellipse. This shape is expected for a mixing layer dominated by roller structures and braids. Along the mixing-layer centreline, the u-velocity fluctuation varies slowly because each individual large-scale structure convects downstream with a nearly constant u-velocity. The $R_{u'u'}$ correlation thus remains high over long distances in the x-direction. There is not a corresponding long correlation distance in the y-direction, however. Along a line of constant x, there are differing fluctuations around the mean u-velocity as the y-location is varied. Thus, $R_{u'u'}$ drops off quickly in the y-direction. For the incompressible mixing layer, the $R_{u'u'} = 0.4$ contour extends from about $\pm 1.4\delta_\omega$ in the x-direction to $+0.4\delta_\omega$ and $-0.7\delta_\omega$ in the y-direction. However, for the weakly compressible mixing layer, the $R_{u'u'} = 0.4$ contour extends from only $\pm 0.8\delta_\omega$ in the x-direction to only $+0.4\delta_\omega$ and $-0.3\delta_\omega$ in the y-direction.

The spatial correlation function $R_{v'v'}$ for the weakly compressible mixing layer as measured by PIV is shown in figure 15, and this can be compared with the corresponding function for an incompressible mixing layer that has been previously presented elsewhere (Olsen & Dutton 2002). Unlike $R_{v'v'}$ for the incompressible mixing layer, which is a vertically oriented ellipse, the correlation field for the weakly compressible mixing layer is essentially circular. This shape is consistent with horizontally oriented elliptical roller structures for the weakly compressible case (see § 3.2.7). For the incompressible mixing layer, which contained circular rollers, the v-velocity at the centre of a roller was zero, but to the right-hand side of the structure the v-velocity quickly became negative, and to the left-hand side of the roller structure the v-velocity quickly became positive. It was this rapid variation in the v-velocity fluctuation that led to short correlation distances in the x-direction for the incompressible case. The circular shape of the $R_{v'v'}$ contours for the weakly compressible mixing layer suggests relatively longer correlation distances of the v-velocity fluctuations in the x-direction. This means that the variation in v-velocity is not as rapid and, thus, there is near-zero v-velocity fluctuation over longer distances in the x-direction, a characteristic found in horizontally oriented elliptical rollers. As was the case for $R_{u'u'}$, the $R_{v'v'}$ correlation field is seen to be smaller for the weakly compressible mixing layer than for the incompressible mixing layer. For the incompressible case, the $R_{v'v'} = 0.4$ contour extends from approximately $\pm 0.5\delta_\omega$ in the x-direction to $+0.6\delta_\omega$ and $-1.0\delta_\omega$ in the y-direction. For the weakly compressible mixing layer, however, the 0.4 contour extends from only about $\pm 0.4\delta_\omega$ in the x- and y-directions.

The question must be addressed as to whether the different shapes and sizes of the correlation functions in the weakly compressible and incompressible cases are a function of the higher Reynolds number in the weakly compressible case or if the different shapes are an effect of compressibility. This can be answered by considering the experimental results of Tung (1982). Tung measured spatial correlations for an incompressible mixing layer using an array of hot wires. In his experiments, $Re_{\delta_\omega} = 4.7 \times 10^4$, which is larger than for the incompressible correlation fields previously measured by us. Comparing the shapes of the correlation fields for the two incompressible experiments shows that the correlation fields have exactly the same shapes. The only effect of increasing the Reynolds number is that the correlation fields become smaller. Thus, it can be concluded that the difference in the shapes of the spatial correlation fields for the weakly compressible mixing layer with respect to those for the incompressible mixing layer are a result of compressibility, not increasing Reynolds number, and the difference in the relative sizes of the correlation functions is a result of the higher Reynolds number in the weakly compressible case.

The spatial correlation function $R_{u'v'}$ is presented for the weakly compressible mixing layer in figure 16. Once again, these spatial correlations are compared with the corresponding correlation for an incompressible mixing layer. In both cases, the $R_{u'v'}$ correlation field is seen to be relatively noisy owing to the small ensemble size. Figure 16 does have a peak value of 0.47 in the centre (i.e. zero displacement), however, which is consistent with the LDV measurements of Goebel & Dutton (1991), and is very similar to the peak value in the incompressible case (0.46). Just as for the other correlation fields presented, $R_{u'v'}$ for the weakly compressible mixing layer appears to be smaller (owing to the higher Reynolds number), and perhaps more horizontally oriented, than its counterpart for the incompressible mixing layer, although quantitative comparisons are difficult because of the irregular shapes.

3.2.7. *Linear stochastic estimation*

It is possible to calculate conditional velocity fields from the spatial correlations using a technique called linear stochastic estimation (Adrian *et al.* 1989). By properly defining the conditions corresponding to a specific large-scale structure, the velocity field representing that structure based on the spatial correlations can be calculated. This was done for the weakly compressible mixing layer by choosing conditions representative of both a roller and a braid. These results are compared to similar calculations performed for an incompressible mixing layer (Olsen & Dutton 2002).

Generally, the event upon which a linear stochastic estimate is based is a velocity fluctuation. Defining rollers and braids in a mixing layer by such an event will not work, however, since the centres of roller structures and braids are characterized by a velocity fluctuation of zero. Thus, the stochastic estimates of both rollers and braids based on a velocity fluctuation will be identical. A different event must be chosen to characterize roller structures and braids.

As discussed earlier, comparison of the individual velocity vector fields to their corresponding vorticity and rate-of-strain fields leads to the conclusion that rollers correspond to peaks in vorticity and braids correspond to peaks in strain. A linear stochastic estimate for mixing-layer structures can then be constructed by incorporating this information. The linear stochastic estimate is based on the local deformation at some location x_0 and is given by

$$\langle u_i'(\boldsymbol{x})|d_{ij}(\boldsymbol{x}_0)\rangle = A_i(\boldsymbol{x}) + B_{ijk}(\boldsymbol{x})d_{jk}(\boldsymbol{x}_0), \tag{5}$$

where d_{jk} is the deformation tensor. The coefficients $A_i(x)$ and $B_{ijk}(x)$ are then calculated by minimizing the mean square error of the estimate. This yields the results

$$A_i(\boldsymbol{x}) = 0, \tag{6}$$

$$\langle u_{j,k}(\boldsymbol{x}_0)u_{l,m}(\boldsymbol{x}_0)\rangle B_{ijk}(\boldsymbol{x}) = \frac{\partial R_{u_l'u_i'}}{\partial \boldsymbol{x}_m}, \tag{7}$$

which is a set of eight equations $(i, l, m = 1, 2)$ that can be solved to obtain $B_{ijk}(x)$. Then, using a given value for the deformation tensor at location x_0, equation (5) can be used to find the linear stochastic estimate of the velocity field.

As a first step in this analysis, several instantaneous vector fields were analysed to find typical deformation tensor values at the centres of both roller structures and braids. For a roller, the deformation tensor is

$$d_{jk} = \begin{vmatrix} -2000 & 50\,000 \\ 20\,000 & 2000 \end{vmatrix},$$

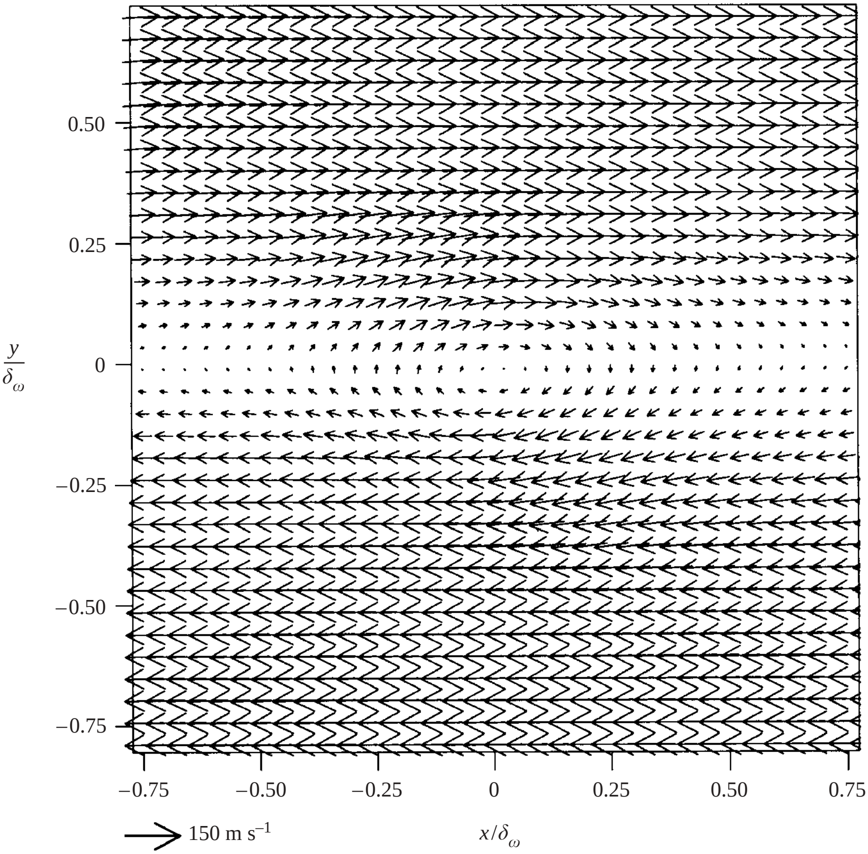

FIGURE 17. Linear stochastic estimate of a roller structure for the weakly compressible mixing layer.

and for a braid, the deformation tensor is

$$d_{jk} = \begin{vmatrix} -1375 & -12\,500 \\ -35\,750 & -1500 \end{vmatrix},$$

where the units are s^{-1}. These values were then used to calculate the linear stochastic estimates of both rollers and braids for the weakly compressible mixing layer.

The linear stochastic estimate for a roller structure in the weakly compressible mixing layer is shown in figure 17. This figure demonstrates that the linear stochastic estimate is an effective technique for determining the features of large-scale structures present in the mixing layer. This is because the linear stochastic estimate behaves like a low-pass filter, eliminating the contributions of small-scale structures (which are very prevalent in the weakly compressible mixing layer owing to the high Reynolds number) and highlighting the underlying large-scale structures.

In figure 17, the linear stochastic estimate of a roller structure in the weakly compressible mixing layer is seen to be elliptical with a horizontal major axis. In contrast, the linear stochastic estimate of a roller in an incompressible mixing layer (Olsen & Dutton 2002) is more circular. This effect of compressibility on roller structures is consistent with the direct numerical simulations of Sandham & Reynolds (1989, 1991), who found that in a compressible mixing layer, vortices are elongated

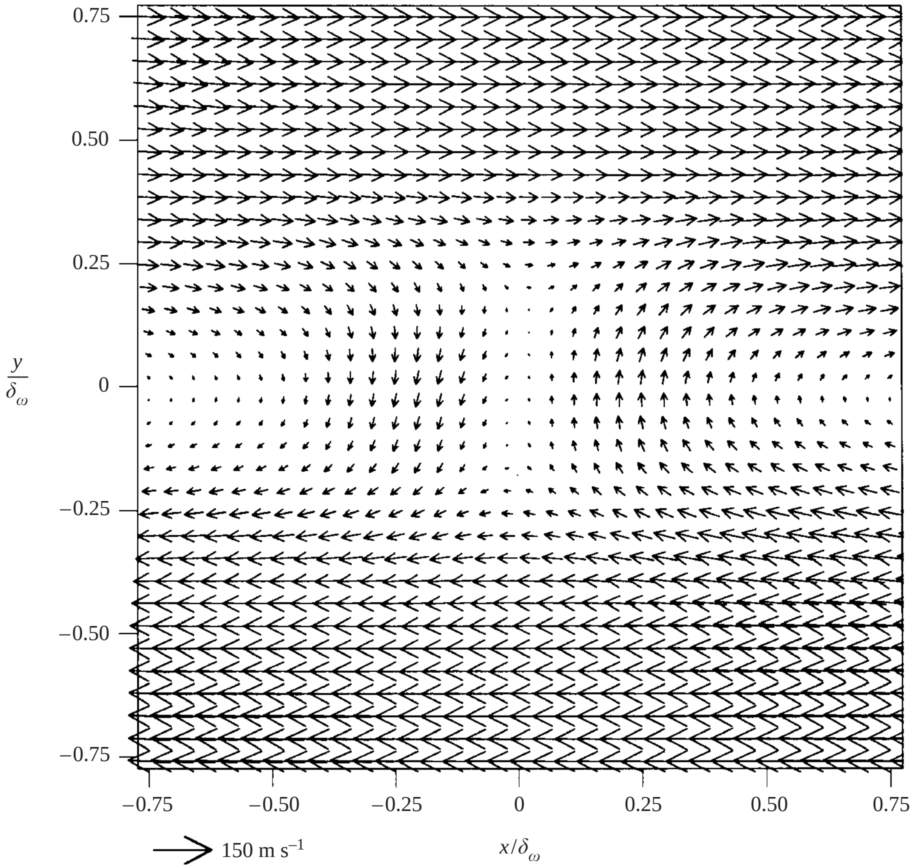

FIGURE 18. Linear stochastic estimate of a braid for the weakly compressible mixing layer.

in the streamwise direction compared to the vortices found in incompressible mixing layers. They also believed that the elongated structures could not entrain as much fluid as the nearly circular structures in incompressible mixing layers, and would thus lead to a smaller growth rate. Indeed, the schlieren photograph presented in figure 3 and also the mean v-velocity profile of figure 10 confirmed that the growth rate of the present weakly compressible mixing is much less than that of a comparable incompressible mixing layer. Thus, it seems that one effect of compressibility is to increase the eccentricity of roller structures, which in turn leads to a diminished mixing-layer growth rate. This elongation of large-scale structures with compressibility also agrees well with the planar Mie scattering visualization results of Messersmith & Dutton (1996). Messersmith & Dutton also observed that the elongated structures are at an angle of about 26° with respect to horizontal. While the conditional roller structure in figure 17 is angled slightly with respect to horizontal, the angle is far less than that measured by Messersmith & Dutton. This can possibly be attributed to Messersmith & Dutton correlating a scalar quantity, whereas the structure in figure 17 is based on correlations of the velocity.

The linear stochastic estimate of a braid structure in a weakly compressible mixing layer is presented in figure 18. Once again, comparison can be made with the linear stochastic estimate of a braid in an incompressible mixing layer (Olsen & Dutton 2002). Both estimates are somewhat similar in appearance, although the incompressible braid is obliquely oriented while the weakly compressible braid is vertically oriented. In addition, in the weakly compressible braid, stagnation occurs along a vertically oriented line, whereas for the incompressible braid, stagnation occurs at a point. Indeed, the braid near the centre of the velocity vector field in figure 4 does appear to have a vertically oriented braid, as the linear stochastic estimate suggests. Clemens & Mungal (1995) also observed a change in braid structure with increasing compressibility in their flow-visualization experiments. In their low convective Mach number case ($M_c = 0.28$), they observed braid structure similar to that found in incompressible mixing layers. However, as the convective Mach number was increased to 0.42, the braid regions developed a 'kink', which became more noticeable as M_c was increased even further. As with Messersmith & Dutton, the results of Clemens & Mungal are based on measurements of a scalar quantity, not velocity. The observed kink in the scalar field may be attributed to changes in the velocity field that manifest themselves as a vertically oriented stagnation region.

4. Conclusions

An ensemble of 37 high-vector density PIV velocity fields was obtained for a weakly compressible mixing layer with $M_c = 0.38$. The individual velocity fields fell into three regimes. The first regime is characterized by large Brown–Roshko-like roller structures that are typical of incompressible mixing layers. The second regime also contains similar structures, but these are smaller than those in the first regime. The third regime of velocity fields showed little, if any, discernible large-scale structure. This observation of intermittent and disorganized large-scale structure is consistent with previous flow-visualization studies. Pairing of roller structures also seemed to occur, but unlike in an incompressible mixing layer, for which the pairing mechanism involves rotation of the two interacting roller structures, pairing in the weakly compressible mixing layer seems to occur through a 'slapping' mechanism, with little transverse movement of the two interacting rollers.

The planar velocity fields were also reduced to a single transverse profile to yield reliable velocity statistics. The peak values of $\langle u' \rangle / \Delta U$, $\langle v' \rangle / \Delta U$ and $\langle u'v' \rangle / (\Delta U)^2$ were found to be 0.19, 0.13 and −0.010, respectively. These agree well with the results of previous LDV experiments by Goebel & Dutton (1991) and PIV experiments of Urban & Mungal (1997, 1998) and Urban *et al.* (1998), and demonstrate the effects of compressibility on the mixing-layer statistical quantities. These effects are that the transverse turbulence intensity and Reynolds shear stress are suppressed, while the streamwise turbulence intensity remains constant with increasing convective Mach number.

The planar velocity data were also used to calculate the spatial correlation fields of velocity fluctuations for the weakly compressible mixing layer. The $R_{u'u'}$ correlation is elliptical with a streamwise-oriented major axis. This is similar to the shape seen in the $R_{u'u'}$ correlation for an incompressible mixing layer. The $R_{v'v'}$ correlation is nearly circular. This is very different from the same correlation for an incompressible mixing layer, which is a vertically oriented ellipse. The $R_{u'v'}$ correlation is somewhat noisier than the other two correlations, most probably due to the limited ensemble size, but appears to be circular with a peak value of 0.47 at the origin. The shapes of these correlation functions suggest flattened elliptical roller structures with the major axis oriented in the streamwise direction. The changes in the shapes of the correlation functions in the weakly compressible case are believed to be a result of compressibility and not of higher Reynolds number. The correlation fields for the weakly compressible mixing layer decay more quickly with increased displacement from the basis points than those found in an incompressible mixing layer. This is to be expected, as the Reynolds number was much greater for the weakly compressible mixing layer than for the incompressible case.

Finally, linear stochastic estimation yielded insights into the characteristics of the large-scale structures found in the weakly compressible mixing layer, and the effects of compressibility on these structures. In the weakly compressible case, the linear stochastic estimate of a roller is a flattened, elliptical structure with a horizontal major axis. This differs from the linear stochastic estimate for an incompressible mixing layer, which was less eccentric. Increasing eccentricity in roller structure shape with increasing compressibility has been observed in previous flow visualization and computational work. The linear stochastic estimate of a braid in the weakly compressible mixing layer is vertically oriented, as opposed to the estimate of a braid for the incompressible case, which was obliquely oriented. Also, the braid in the weakly compressible mixing layer has a vertically oriented stagnation line, whereas in the incompressible case, stagnation was seen to occur at a point. This is consistent with earlier flow visualization work which also showed changes in braid structure with increasing compressibility.

Support for this work was provided by the US Army Research Office (Grant no. DAAG55-97-1-0122) with Dr Thomas L. Doligalski as monitor. The authors also thank Professor Ronald J. Adrian for his help in formulating the linear stochastic estimation results.

REFERENCES

Adrian, R. J., Jones, B. G., Chung, M. K., Nithianandan, C. K. & Tung, A. T.-C. 1989 Approximation of turbulent conditional averages by stochastic estimation. *Phys. Fluids* A **1**, 992–996.

Bloomberg, J. E. 1989 An investigation of particle dynamics effects related to LDV measurements in compressible flows. MS thesis, University of Illinois.

Bogdanoff, D. W. 1982 Compressibility effects in turbulent shear layers. *AIAA J.* **21**, 926–927.

Bogdanoff, D. W. 1984 Interferometric measurement of heterogeneous shear layer spreading rates. *AIAA J.* **22**, 1550–1555.

Browand, F. K. & Latigo, B. O. 1979 Growth of the two-dimensional mixing layer from a turbulent and nonturbulent boundary layer. *Phys. Fluids* **22**, 1011–1019.

Brown, G. L. & Roshko, A. 1974 On density effects and large structure in turbulent mixing layers. *J. Fluid Mech.* **64**, 775–814.

Chinzei, N., Masuaya, G., Komuro, T. & Kudou, K. 1986 Spreading of two-stream supersonic turbulent mixing layers. *Phys. Fluids* **29**, 1345–1347.

Clemens, N. T. & Mungal, M. G. 1992 Two- and three-dimensional effects in supersonic mixing layers. *AIAA J.* **30**, 973–981.

Clemens, N. T. & Mungal, M. G. 1995 Large-scale structure and entrainment in the supersonic mixing layer. *J. Fluid Mech.* **284**, 171–216.

Day, M. J., Reynolds, W. C. & Mansour, N. N. 1998 The structure of the compressible reacting mixing layer: insights from linear stability analysis. *Phys. Fluids* **10**, 993–1007.

Dutton, J. C. 1997 Compressible turbulent free shear layers. *AGARD/VKI Special Course on Turbulence in Compressible Flows*, *AGARD Rep.* 819. Rhodes St Genese, Belgium.

Elliott, G. S. & Samimy, M. 1990 Compressibility effects in free shear layers. *Phys. Fluids* **2**, 1231–1239.

Elliott, G. S., Samimy, M. & Arnette, S. A. 1992 Study of compressible mixing layers using filtered Rayleigh scattering based visualizations. *AIAA J.* **30**, 2567–2569.

ELLIOTT, G. S., SAMIMY, M. & ARNETTE, S. A. 1995 The characteristics and evolution of large-scale structures in compressible mixing layers. *Phys. Fluids* **7**, 864–876.

FREUND, J. B., MOIN, P. & LELE, S. K. 1997 Compressibility effects in a turbulent annular mixing layer. *Rep.* TF-72. Flow Physics and Computation Division, Department of Mechanical Engineering, Stanford University.

GOEBEL, S. G. & DUTTON, J. C. 1991 Experimental study of compressible turbulent mixing layers. *AIAA J.* **29**, 538–546.

GROSCH, C. E. & JACKSON, T. L. 1991 Inviscid spatial stability of a three-dimensional compressible mixing layer. *J. Fluid Mech.* **231**, 35–50.

IKAWA, H. & KUBOTA, T. 1974 Investigation of supersonic turbulent mixing layer with zero pressure gradient. *AIAA J.* **13**, 566–572.

JOHNSON, D. A. 1971 An investigation of the turbulent mixing layer between two parallel gas streams of different composition and density with a laser doppler velocimeter. PhD thesis, University of Missouri.

MAHADEVAN, R. & LOTH, E. 1994 High-speed cinematography of compressible mixing layers. *Exps. Fluids* **17**, 179–189.

MESSERSMITH, N. L. & DUTTON, J. C. 1996 Characteristic features of large structures in compressible mixing layers. *AIAA J.* **34**, 1814–1821.

MESSERSMITH, N. L., GOEBEL, S. G., FRANTZ, W. H., KRAMMER, E. A., RENIE, J. P., DUTTON, J. C. & KRIER, H. 1988 Experimental and analytical investigations of supersonic mixing layers. *AIAA Paper* 88-0702.

NELSON, C. & MENON, S. 1998 Unsteady simulations of compressible spatial mixing layers. *AIAA Paper* 98-0786.

OLSEN, M. G. 1999 Planar velocity measurements in an incompressible and a weakly compressible mixing layer. PhD thesis, University of Illinois.

OLSEN, M. G. & DUTTON, J. C. 2002 Stochastic estimation of large structures in an incompressible mixing layer. *AIAA J.* **40**, 2431–2438.

PAPAMOSCHOU, D. 1991 Structure of the compressible turbulent shear layer. *AIAA J.* **29**, 680–681.

PAPAMOSCHOU, D. & ROSHKO, A. 1988 The compressible turbulent shear layer: an experimental study. *J. Fluid Mech.* **197**, 453–477.

PRASAD, A. K., ADRIAN, R. J., LANDRETH, C. C. & OFFUTT, P. W. 1988 Measurement and refinement of velocity data using high image density analysis in particle image velocimetry. *Proc. Fourth Intl Symp. on Applications of Laser Anemometry to Fluid Mechanics*, Lisbon, Portugal, pp. 485–497.

RAGAB, S. A. & WU, J. L. 1989 Linear instability waves in supersonic turbulent mixing layers. *AIAA J.* **27**, 677–686.

SAMIMY, M. & ELLIOTT, G. S. 1990 Effects of compressibility on the characteristics of free shear flows. *AIAA J.* **28**, 439–445.

SAMIMY, M. & LELE, S. K. 1991 Motion of particles with inertia in a compressible shear layer. *Phys. Fluids* A **3**, 1915–1923.

SAMIMY, M., REEDER, M. F. & ELLIOTT, G. S. 1992 Compressibility effects on large structures in free shear flows. *Phys. Fluids* A **4**, 1251–1258.

SANDHAM, N. D. & REYNOLDS, W. C. 1989 Compressible mixing layer: linear theory and direct numerical simulation. *AIAA J.* **28**, 618–624.

SANDHAM, N. D. & REYNOLDS, W. C. 1991 Three-dimensional simulations of large eddies in the compressible mixing layer. *J. Fluid Mech.* **224**, 133–158.

TUNG, A. T.-C. 1982 Properties of conditional eddies in free shear flows. PhD thesis, University of Illinois.

URBAN, W. D. & MUNGAL, M. G. 1997 Planar velocity measurements in compressible mixing layers. *AIAA Paper* 97-0757.

URBAN, W. D. & MUNGAL, M. G. 1998 A PIV study of compressible mixing layers. *Proc. Ninth Intl Symp. on Applications of Laser Techniques to Fluid Mechanics, Lisbon, Portugal*, pp. 17.1.1–17.1.8.

URBAN, W. D., WATANABE, S. & MUNGAL, M. G. 1998 Velocity field of the planar shear layer: compressibility effects. *AIAA Paper* 98-0697.

VREMAN, A. W., SANDHAM, N. D. & LUO, R. H. 1996 Compressible mixing layer growth rate and turbulence characteristics. *J. Fluid Mech.* **320**, 235–258.